# Detection of wavelength shift of near-infrared laser using mechanical microresonator-based sensor with Si-covered gold nanorods as optical absorber

Sugano, Koji ; Tanaka, Yuki ; Uesugi, Akio ; Maeda, Etsuo ; Kometani, Reo ; Isono, Yoshitada

(Citation)
Sensors and Actuators A: Physical,315:112337

(Issue Date)
2020-11-01

(Resource Type)
journal article

(Version)
Accepted Manuscript

# Detection of wavelength shift of near-infrared laser using mechanical microresonator-based sensor with Si-covered gold nanorods as optical absorber

Koji Sugano[a], Yuki Tanaka[a], Akio Uesugi[a], Etsuo Maeda[b], Reo Kometani[b,c], and Yoshitada Isono[a]

a Department of Mechanical Engineering, Graduate School of Engineering, Kobe University, 1-1 Rokkodai-cho, Nada-ku, Kobe 657-8501 JAPAN
b Department of Mechanical Engineering, Graduate School of Engineering, The University of Tokyo, 7-3-1 Hongo, Bunkyo-ku, Tokyo 113-8654 JAPAN
c Department of Human & Engineered Environmental Studies, Graduate School of Frontier Sciences, The University of Tokyo, 5-1-5 Kashiwanoha, Kashiwa-shi, Chiba 277-8563 JAPAN

Corresponding author: Koji Sugano, sugano@mech.kobe-u.ac.jp

Keywods: micromechanical resonator; resonant frequency; near-infrared laser; plasmonic absorber; gold nanorod

## *Abstract*

This study presents a micromechanical resonator to detect near-infrared (NIR) laser wavelength shifts for dense wavelength division multiplexing (DWDM) systems. A feedback control of laser wavelength detecting the wavelength shift is required to keep a spacing of adjacent wavelength channel. The conventional detection method with an etalon filter has the detectable limit of wavelength shift. In this regard, we integrate a micromechanical resonator with plasmonic gold nanorod structures to produce the optical absorption change due to the wavelength shift. The wavelength shift can be detected via the resonant frequency shift based on the thermal stress change in the resonator. The gold nanorod array is fabricated on a gold thin film and subsequently covered by a Si thin film, which is used for controlling the refractive index of the surrounding medium. This causes absorption peaks of plasmonic resonance to be generated in the NIR region. We develop a theoretical equation for the relative resonant frequency that is in proportion to the laser intensity and the beam length cubed. The experimental tendency of relative resonant frequency shifts is observed to be in good agreement with the theoretical equation. The maximum relative resonant frequency shift is 69 Hz/nm, whereas the resolution is estimated to be 0.37 pm, taking into account the thermomechanical noise. Therefore, the fabricated resonator is confirmed to be useful for measuring the laser wavelength with high resolution for large-capacity DWDM systems.

## 1. Introduction

Micromechanical resonators are used for highly sensitive mass, thermal, inertia, and pressure sensors because of their high-sensitivity resonator characteristics such as resonant frequency [1-5]. For example, a temperature change of a micromechanical resonator results in a resonant frequency change due to the thermal stress of the resonator beam. Therefore, this phenomenon is used for detecting heat applied to the resonator beam [6-11].

This study focuses on the application of micromechanical resonators to detection of wavelength shift of near-infrared (NIR) laser, integrating a resonator with a plasmonic absorber. Gold nanostructures offer optical absorption peaks in a spectrum owing to surface plasmon resonance. Gold nanorods are one of the candidates for plasmonic nanostructures. They enable adjusting the absorption peak wavelength through the nanostructure dimensions such as width, length, and pitch, as well as the surrounding media [12-29]. Different absorptions are obtained depending on the laser wavelength of NIR light. Therefore, a laser wavelength shift can be detected by the resonant frequency shift because of the absorption (temperature) change of the resonator beam; details are described in Section 2.

Detecting the wavelength shift is useful for a dense wavelength division multiplexing (DWDM) system, where a large number of wavelength channels ranging from approximately 1530 to 1625 nm are present [30]. The telecommunication standardization sector of the international telecommunication union provides the channel spacing standard, which is 0.8 (100), 0.4 (50), 0.2 (25), or 0.1 nm (12.5 GHz). The conventional system detects the wavelength shift by measuring the laser intensity change through an etalon filter that has wavelength depending transmittance [30, 31]. Laser light from a source is divided into two paths using a beam splitter. One path is used for laser power monitoring with a photodetector. Another path is used for wavelength monitoring through an etalon filter as a wavelength discriminator [31-35]. The detection resolution of the conventional system is insufficient for a channel spacing of 0.1 nm due to limitation of processing accuracy; it has been used for a channel spacing of 0.4 or 0.8 nm. Therefore, to realize enough resolution of wavelength detection is still challenging for a reliable system with a 0.1-nm spacing, requiring a 2.5 pm resolution.

In this study, we fabricated and evaluated a mechanical resonator device with a gold nanorod array for the detecting laser wavelength shifts to realize the wavelength detection resolution of less than 2.5 pm. It is thought that the device performance depends on the laser intensity and the resonator beam dimension, such as the beam length. Therefore, we study the effect of these parameters on the resonant frequency shift. Finally, the theoretical resolution of the measurement device is estimated, taking into account the thermal-mechanical noise.

## 2. Theory and experiments

### *2.1 Theoretical equations*

Metal nanostructures, such as gold, silver, and aluminum, have surface plasmon resonance, resulting in a unique optical absorption characteristic, which is to show the absorption peaks in a spectrum. Therefore, changes of the absorption $\beta$ in a laser, defined as $\Delta\beta = \beta_2 - \beta_1$, are obtained during the shift of the wavelength $\lambda$ as $\Delta\lambda = \lambda_2 - \lambda_1$. In this study, the gold nanorod array was placed at the center of the doubly-clamped micro-oscillator beam, fabricated from the silicon-on-insulator (SOI) wafer, to function as an optical absorber, as shown in Fig. 1(a). The beam temperature changes with the absorption change, while thermal stress applies to the beam. The thermal stress change results in a resonant frequency shift. In this study, therefore, we propose to detect the wavelength shift from the resonant frequency shift.

The following equations were obtained for the beam temperature and resonant frequency. Equations (1) and (2) give the temperature $T(x)$ along in the longitudinal direction of the beam and the mean temperature change $\Delta T$, respectively.

$$T(x) = T_0 + \frac{(L/2 - |x|)\beta P}{2\kappa b h} \ , \tag{1}$$

$$\Delta T = \int_{-L/2}^{L/2} \frac{(L/2 - |x|)\beta P}{\kappa b h} \frac{dx}{L} = \frac{L \Delta \beta P}{8 b h \kappa} \ , \tag{2}$$

where $T_0$ is the original temperature before laser irradiation, $\kappa$ is the thermal conductivity of Si, and $P$ is the laser intensity. As shown in Fig. 1(a), $b$, $h$, and $L$ indicate the beam width, thickness, and length, respectively. Note that, in Eq. (1), $T_0$ is the temperature where the fixed end is established, $x$ ranges from $L/2$ to $-L/2$.

The temperature change occurs when shifting the laser wavelength owing to the absorption change ($\Delta\beta$). The resonant frequency ($f_\sigma$) under thermal stress of the beam is given by Eq. (3) [36-39].

$$f_\sigma = f_0 \sqrt{1 + \frac{3}{\pi^2} \cdot \frac{\sigma L^2}{E h^2}} = f_0 \sqrt{1 - \frac{3}{\pi^2} \cdot \frac{\alpha L^3 \beta P}{8 h^3 b \kappa}} \approx f_0 \left(1 - \frac{3}{\pi^2} \cdot \frac{\alpha L^3 \beta P}{16 h^3 b \kappa}\right) \ . \tag{3}$$

The resonant frequency under no laser irradiation $f_0$ is given by $f_0 = 1.03t/L^2\sqrt{E/\rho}$, where $E$ is the Young's modulus, $\rho$ is the density, and $\alpha$ is the thermal expansion coefficient. The change in thermal stress ($\Delta\sigma = -\alpha E \Delta T$) causes the resonant frequency shift $\Delta f$. The relative resonant frequency shift is calculated as follows.

$$\frac{\Delta f}{f_{\sigma 1}} = \frac{f_{\sigma 1} - f_{\sigma 2}}{f_{\sigma 1}} \approx \frac{3}{\pi^2} \cdot \frac{\alpha L^3 P}{16 h^3 b \kappa} \Delta\beta \ . \tag{4}$$

From Eq. (4), we found that the relative resonant frequency shift is linearly proportional to the absorption change $\Delta\beta$, which depends on the laser wavelength shift $\Delta\lambda$. We note that the relative resonant frequency shift increases with the laser intensity $P$ and the beam length cubed $L^3$.

### *2.2 Device structure and fabrication*

The beam was fabricated from the SOI wafer via the standard microfabrication process, and the gold nanorod absorber at the beam center was fabricated via an electron-beam (EB) lithography-based process. The gold nanorod length and width were designed to be 500 nm and 50 nm. The nanorods were arranged on a gold thin film of 100 nm thickness, and the pitches were of 1500 nm and 200 nm. As shown in Fig. 1(c), the thickness of the Si thin film on the gold nanorods was 100 nm to generate the absorption peak at the target wavelength of approximately 1550 nm in the absorption spectrum. The absorption peaks can be adjusted by the refractive index of the surrounding medium. In this study, Si was used as the surrounding medium covering gold nanorods. The peak wavelength in the absorption spectrum shifts with the surrounding dielectric constant [12-29].

The thicknesses of the device layer, the buried oxide (BOX) layer, and the handle substrate are of 2 µm, 0.5 µm, and 450 µm, respectively. (1) A 10 µm × 10 µm gold pad with a thickness of 100 nm was fabricated on the device layer by electron-beam (EB) vacuum evaporation and a subsequent lift-off process. (2) Gold nanorods were fabricated on the gold pad by EB lithography, EB vacuum evaporation, and a subsequent lift-off process in the region of 7 μm × 7 μm. (3) After that, the deep hole was fabricated from the backside for the through-hole. Subsequently, the device layer etching was performed for the beam structure. (4) The BOX layer was removed from the backside opening. Hence, the length of the backside opening determines the resonator beam length. Five types of resonators with different beam lengths were fabricated. (5) A Si was sputtered on the resonator beam to form a Si thin film.

### *2.3 Analytical and theoretical methods*

To validate the theoretical equations and the properties on beam temperature, we performed thermal analysis using the finite element method (FEM) as well as theoretical calculation. The structure including the BOX layer and the substrate, as shown in Fig. 1, was used as the analytical model for FEM simulation. The temperature at the substrate bottom was fixed at the initial temperature of $T_0 = 300$ K. The irradiating area of 10 μm × 10 μm, which is equal to the dimension of the gold pad, was set at the beam center as an absorber pad. A heat quantity of $\beta P$ was applied to the absorber pad.

### *2.4 Experimental methods*

We measured the reflection spectrum of the absorber $R(\lambda)$ and calculated the absorption spectrum $A(\lambda)$ from the measurement results with $A(\lambda) = 1 - R(\lambda),$ assuming that the transmission is 0 due to the 100-nm-thick gold thin film. A 100-nm-thick flat gold thin film on a Si substrate was used as a reference. The wavelength interval was set to 1 nm.

The vibration measurements were performed using a laser Doppler vibrometer (MLD-230V-100, NEOARK Corporation, Japan) equipped with 633-nm-wavelength He-Ne laser, as shown in Fig. 2. The device chip was put in a vacuum chamber at less than $10^{-3}$ Pa environment. The NIR evaluation laser irradiates the absorber with the adjusted wavelength from 1548 to 1562 nm. The wavelength interval was set to 2 nm. We use the 488-nm-wavelength semiconductor laser for a laser oscillation applying a sinusoidal voltage.

## 3. Results and discussions

### *3.1 Analytical and theoretical results*

Figure 3 shows the longitudinal temperature distribution of the beam calculated using Eq. (1) (solid lines) and FEM (dotted lines) depending on the beam length. In these calculations, $T_0$, $\beta P$, $\kappa$, $b$ and $h$ were set to 300 K, 0.4 mW, 156 W/m·K, 20 μm, and 2 μm, respectively.

The slopes of the temperature distribution are theoretically determined by $\beta P/\kappa bh$ not depending on the beam length. The maximum temperature appears at the center of the beam (laser irradiation position). The average temperature differences from $T_0$ were calculated to be 1.6, 1.2, 0.99, 0.80, and 0.59 K for the beam lengths of 200, 150, 125, 100, and 75 μm, respectively. Equation (2) shows that $\Delta T$ proportionally increased with the beam length.

The slope of the temperature distribution calculated by FEM analysis was the same for the theoretical calculation. We found the different shapes of the temperature distribution at the beam center because of the absorption pad. The pad size is much smaller than the beam length. Therefore, the different shape at the beam center has little effect on the average beam temperature. The temperature difference from $T_0$ at the fixed ends was simulated to be 0.28 K. The average temperature differences from $T_0$ were calculated to be 1.9, 1.5, 1.3, 1.1, and 0.87 K for the beam lengths of 200, 150, 125, 100, and 75 μm, respectively. The difference between the theoretical and the simulated results corresponds to the temperature at the fixed end. The temperature difference $\Delta T$ was proportional to the beam length as well as the theoretical calculation.

### *3.2 Fabrication result*

Figure 4 shows the images from the scanning electron microscopy (SEM). The beam length was 188 μm in this case, shown in Fig. 4(a). We measured the length of 5 devices with different lengths of 200, 150, 100, 75, and 50 μm, as designed, while the lengths of the fabricated beam were 188, 134, 112, 86, and 62 μm, respectively. The absorber pad was observed at the beam center. Figures 4(b)-(d) show the gold nanorod array. We successfully fabricated the gold nanorods covered with the Si thin film. The mean length and width of the nanorods were 501 nm and 67 nm, respectively. The mean thickness of the sputtered Si film was measured to be 61 nm.

### *3.3 Absorption spectra*

The gold nanorod array in the presence of the Si thin film shows the peaks of absorption in the wavelength from approximately 1400 nm to 1700 nm, as shown in Fig. 5(a-i). The structure without gold nanorods in the presence of the Si thin film, the flat structure of the Si thin film on the gold thin film, exhibited no absorption peak and a gradual increase of the absorption with the wavelength, as shown in Fig. 5(a-ii). The gradual increase was caused by optical interference depending on the thickness of the Si thin film. For the gold nanorod array, in the absence of the Si thin film, the absorption was low without peaks, as shown in Fig. 5(a-iii). We confirmed that the Si thin film and the gold nanorods were the valid structure for generating an absorption peak at approximately 1560 nm, as shown in Fig. 5(b). The absorptions at 1548 nm and 1562 nm were 0.376 and 0.395, respectively, resulting in an absorption difference of 0.019.

### *3.4 Resonant frequencies*

As shown in Fig. 6, the experimental resonant frequency as a function of the beam length under no NIR laser irradiation agreed with the calculation results, which were proportional to $1/L^2$ according to the theoretical equation. Figure 7 shows the resonant curves, with and without irradiation by the 1-mW evaluation laser, at a beam length of 188 μm. A Lorentzian function was used for the fitting curve. The resonant frequencies with and without the evaluation laser irradiation at a wavelength of 1548 nm were 462.2 kHz and 463.6 kHz, respectively. We confirmed that the resonant frequency shifted with the laser irradiation and laser wavelength shift. Figure 8 shows the resonant frequency depending the laser wavelength for a beam length of 188 μm and a laser intensity of 1 mW. A large resonant frequency shift was observed by varying the laser wavelength in the range from 1548 to 1562 nm. However, the beam without the absorber exhibited small shifts because of small absorption slopes. The resonant frequency decreased with increasing the laser wavelength because the absorption increased with increasing the laser wavelength in the range from 1548 to 1562 nm, as shown in Fig. 5. The maximum relative resonant frequency per wavelength shift was 68.8 Hz/nm when the wavelength varied from 1552 to 1554 nm.

The relative resonant frequency shift depending on the laser wavelength is shown in Fig. 9. The relative resonant frequency shift was calculated from the experimental results based on the resonant frequency at 1548 nm using $\Delta f/f_{\sigma 0} = \left(f_{\sigma 0} - f_\sigma(\lambda)\right)/f_{\sigma 0}$, according to Eq. (4). Here, $f_{\sigma 0}$ and $f_\sigma(\lambda)$ are the resonant frequencies at evaluation laser wavelengths of 1548 and $\lambda$ nm, respectively. The relative resonant frequency shifts for all the cases when the beam length increased with the laser wavelength. As shown in Figs. 9 and 10, the relative resonant frequency shift increased with the beam length. In Fig. 10, the dotted line indicates the fitting curve proportional to the beam length cubed ($L^3$). The experimental result agreed with the theoretical tendency of Eq. (4). We confirmed that the beam length is a significantly effective parameter for the device design. In a similar fashion, it is expected that the beam thickness is also significantly effective parameter to improve the sensitivity due to the proportional relationship to the beam thickness cubed ($t^3$) according to Eq. (4). The resonant frequency linearly decreases with increasing the laser intensity ranging from 0 to 3 mW for a beam length of 188 μm and a laser wavelength of 1548 nm, as shown in Fig. 11. This tendency was consistent with Eq. (3) as a function of laser intensity $P$. The theoretical equation was validated under the experimental condition used in this study. The temperature at the fixed end of the beam was set constant, for example, $T_0 = 300$ K, as the initial temperature for all beam lengths in the temperature calculation using Eq. (1) as shown in Fig. 3. The good agreement between the experimental results and the theoretical equation indicates that the fixed end temperatures were almost the same for all beam lengths in the experiments, which is because the heat of the beam escapes through a BOX layer for keeping the fixed end temperature constant. The experiments verified the assumption for developing the equations. We confirmed that the equations were useful for the device design.

### *3.5 Detection resolution*

Next, we calculated the resolution of the wavelength detection taking into account the thermal-mechanical noise [40]. The resolution $\delta f$ is given by,

$$\delta f = \frac{1}{2\pi}\sqrt{\frac{k_B T \Delta w}{2\pi f_0 M_{eff} \langle {x_c}^2 \rangle \mathrm{Q}}} \quad . \tag{5}$$

where $k_B$ the Boltzmann's constant, $\Delta w$ the bandwidth of the vibration measurement system used in this study, $M_{eff}$ an effective mass, and $x_c$ the critical vibration amplitude. The Q factor was 1522 for a beam length of 188 μm when a laser intensity of 1 mW and a laser wavelength of 1552 nm were used. The resolution was estimated to be 0.37 pm using the maximum shift rate of 69 Hz/nm. The result shows high sensitivity for the wavelength detection for a reliable DWDM system and several applications to optical sensing.

## 4. Conclusion

This study developed a micromechanical resonator integrated with an optical absorber of Si-covered gold nanorod array for the detection of laser wavelength shifts of NIR regions ranging from 1548 nm to 1562 nm. The laser wavelength shift was detected from the resonant frequency shift of the resonator due to the temperature and thermal stress changes. The Si-covered gold nanorod array exhibited the wavelength depending absorption such that the wavelength shift caused the temperature change. Moreover, we fabricated a doubly clamped micromechanical resonator with the absorber. We observed that the fabricated absorber showed the absorption peak at the wavelength ranging from approximately 1400 to 1700 nm. The resonant frequency decreased when the absorption increased, indicating a wavelength increment, according to the measured absorption spectrum. The relative resonant frequency shift was in proportion to the laser intensity (*P*=0-3 mW) and the beam length cubed (*L*=62-188 μm). The maximum resonant frequency shift was 69 Hz/nm when using a 188-μm long resonator. The tendency of the experimental results exhibits good agreement with the theoretical equations. The measured Q factor was 1522 at the laser intensity of 1 mW and the beam length of 188 μm. The detection resolution of the wavelength shift was estimated to be 0.37 pm using the equation considering the thermal-mechanical noise. The detection resolution is expected to be improved by longer and thinner resonator beam according to the validated theoretical equation. The results of this study enable us to detect the laser wavelength shift of approximately 1550 nm with high wavelength resolution for reliable large-capacity DWDM systems.

## Conflicts of interest

The authors declare no conflict of interest.

## Acknowledgement

A part of this study was supported by Micro/Nano Fabrication Hub in Kyoto University funded by the Ministry of Education, Culture, Sports, Science and Technology (MEXT), Japan. A part of this study was supported by JSPS KAKENHI Grant Number JP18H01847.

## References

[1] Z. An, M. Esashi, T. Ono, Piezoresistive Silicon Microresonator for Measurements of Hydrogen Adsorption in Carbon Nanotubes, Jpn. J. Appl. Phys., 51 (2012) 116601.

[2] T. Ono, M. Esashi, Mass sensing with resonating ultra-thin silicon beams detected by a double-beam laser Doppler vibrometer, Meas. Sci. Technol., 15 (2004) 1977-1981.

[3] K.L. Ekinci, M.L. Roukes, Nanoelectromechanical systems, Rev. Sci. Instrum., 76 (2005) 061101.

[4] T. Ono, X. Li, H. Miyashita, M. Esashi, Mass sensing of adsorbed molecules in sub-picogram sample with ultrathin silicon resonator, Rev. Sci. Instrum., 74 (2003) 1240.

[5] K.L. Ekinci, X.M.H. Huang, M.L. Roukes, Ultrasensitive nanoelectromechanical mass detection, Appl. Phys. Lett., 84 (2004) 4469-4471.

[6] N. Inomata, K. Saito, T. Ono, Q factor enhancement of Si resonator by nonlinear damping, Microsyst. Technol., 23 (2016) 1201-1205.

[7] M. Toda, N. Inomata, T. Ono, I. Voiculescu, Cantilever beam temperature sensors for biological applications, IEEJ Transactions on Electrical and Electronic Engineering, 12 (2017) 153-160.

[8] M. Toda, T. Otake, H. Miyashita, Y. Kawai, T. Ono, Suspended bimaterial microchannel resonators for thermal sensing of local heat generation in liquid, Microsyst. Technol., 19 (2012) 1049-1054.

[9] N. Inomata, T. Ono, Thermal Sensor Probe with a Si Resonator in a Cavity for Thermal Insulation, Jpn. J. Appl. Phys., 52 (2013) 117201.

[10] E. Maeda, R. Kometani, Sub-picometer multi-wavelength detector based on highly sensitive nanomechanical resonator, Appl. Phys. Lett., 111 (2017) 013102.

[11] K. Takegami, K. Nakafuji, N. Arai, A. Uesugi, K. Sugano, Y. Isono, Effect of clamped beam pattern on resonant frequency shift of microresonator under near-infrared laser irradiation, Jpn. J. Appl. Phys., 59 (2020) SIII04.

[12] P.K. Jain, K.S. Lee, I.H. El-Sayed, M.A. El-Sayed, Calculated absorption and scattering properties of gold nanoparticles of different size, shape, and composition: applications in biological imaging and biomedicine, J. Phys. Chem. B, 110 (2006) 7238-7248.

[13] S. Link, M. Mohamed, M. El-Sayed, Simulation of the optical absorption spectra of gold nanorods as a function of their aspect ratio and the effect of the medium dielectric constant, J. Phys. Chem. B, 103 (1999) 3073-3077.

[14] Y.-Y. Yu, S.-S. Chang, C.-L. Lee, C.C. Wang, Gold nanorods: electrochemical synthesis and optical properties, J. Phys. Chem. B, 101 (1997) 6661-6664.

[15] O.L. Muskens, G. Bachelier, N.D. Fatti, F. Vallee, A. Brioude, X. Jiang, M.-P. Pileni, Quantitative absorption spectroscopy of a single gold nanorod, J. Phys. Chem. C, 112 (2008) 8917-8921.

[16] K. Ueno, S. Juodkazis, M. Mino, V. Mizeikis, H. Misawa, Spectral sensitivity of uniform arrays of gold nanorods to dielectric environment, J. Phys. Chem. C, 111 (2007) 4180-4184.

[17] M. Autore, P. Li, I. Dolado, F.J. Alfaro-Mozaz, R. Esteban, A. Atxabal, F. Casanova, L.E. Hueso, P. Alonso-Gonzalez, J. Aizpurua, A.Y. Nikitin, S. Velez, R. Hillenbrand, Boron nitride nanoresonators for phonon-enhanced molecular vibrational spectroscopy at the strong coupling limit, Light Sci Appl, 7 (2018) 17172.

[18] W.L. Barnes, A. Dereux, T.W. Ebbesen, Surface plasmon subwavelength optics, nature, 424 (2003) 824-830.

[19] W. Chen, T. Kan, Y. Ajiki, K. Matsumoto, I. Shimoyama, NIR spectrometer using a Schottky photodetector enhanced by grating-based SPR, Opt. Express, 24 (2016) 25797-25804.

[20] X. Duan, G. Zhou, Y. Huang, Y. Shang, X. Ren, Theoretical analysis and design guideline for focusing subwavelength

gratings, Opt. Express, 23 (2015) 2639-2646.

[21] T. Iqbal, Coupling Efficiency of Surface Plasmon Polaritons: Far- and Near-Field Analyses, Plasmonics, 12 (2016) 215-221.

[22] T. Iqbal, S. Afsheen, Coupling Efficiency of Surface Plasmon Polaritons for 1D Plasmonic Gratings: Role of Under- and Over-Milling, Plasmonics, 11 (2016) 1247-1256.

[23] T. Ongarello, F. Romanato, P. Zilio, M. Massari, Polarization independence of extraordinary transmission trough 1D metallic gratings, Opt. Express, 19 (2011) 9426-9433.

[24] F. Romanato, T. Ongarello, G. Zacco, D. Garoli, P. Zilio, M. Massari, Extraordinary optical transmission in one-dimensional gold gratings: near-and far-field analysis, Appl. Opt., 50 (2011) 4529-4534.

[25] I.S. Spevak, A.Y. Nikitin, E.V. Bezuglyi, A. Levchenko, A.V. Kats, Resonantly suppressed transmission and anomalously enhanced light absorption in periodically modulated ultrathin metal films, Physical Review B, 79 (2009).

[26] T. Wang, V.H. Nguyen, A. Buchenauer, U. Schnakenberg, T. Taubner, Surface enhanced infrared spectroscopy with gold strip gratings, Opt. Express, 21 (2013) 9005-9010.

[27] S. Xiao, J. Zhang, L. Peng, C. Jeppesen, R. Malureanu, A. Kristensen, N.A. Mortensen, Nearly zero transmission through periodically modulated ultrathin metal films, Appl. Phys. Lett., 97 (2010) 071116.

[28] Y. Xie, A. Zakharian, J.V. Moloney, M. Mansuripur, Transmission of light through periodic arrays of sub-wavelength slits in metallic hosts, Opt. Express, 14 (2006) 6400-6413.

[29] P. Zilio, D. Sammito, G. Zacco, F. Romanato, Absorption profile modulation by means of 1D digital plasmonic gratings, Opt. Express, 18 (2010) 19558-19565.

[30] G.E. Keiser, A review of WDM technology and applications, Opt. Fiber Technol., 5 (1999) 3-39.

[31] Y. Yoon, J. Shim, D. Jang, J. Kim, Y. Eo, F. Rhee, Transmission spectra of Fabry-Perot etalon filter for diverged input beams, IEEE Photonics Technol. Lett., 14 (2002) 1315-1317.

[32] A. Frenkel, C. Lin, Angle-tuned etalon filters for optical channel selection in high density wavelength division multiplexed systems, J. Lightwave Technol., 7 (1989) 615-624.

[33] T. Niemi, M. Uusimaa, S. Tammela, P. Heimala, T. Kajava, M. Kaivola, H. Ludvigsen, Tunable silicon etalon for simultaneous spectral filtering and wavelength monitoring of a DWDM transmitter, IEEE Photonics Technol. Lett., 13 (2001) 58-60.

[34] B. Pezeshki, F. Tong, J. Kash, D. Kisker, R. Potemski, Tapered Fabry-Perot waveguide optical demultiplexer, IEEE Photonics Technol. Lett., 5 (1993) 1082-1085.

[35] Z. Zheng, G. Yang, H. Li, X. Liu, Three-stage Fabry–Perot liquid crystal tunable filter with extended spectral range, Opt. Express, 19 (2011) 2158-2164.

[36] A. Bokaian, Natural frequencies of beams under compressive axial loads, J. Sound Vib., 126 (1988) 49-65.

[37] A. Bokaian, Natural frequencies of beams under tensile axial loads, J. Sound Vib., 142 (1990) 481-498.

[38] S.C. Jun, X.M.H. Huang, M. Manolidis, C.A. Zorman, M. Mehregany, J. Hone, Electrothermal tuning of Al–SiC nanomechanical resonators, Nanotechnology, 17 (2006) 1506-1511.

[39] H. Okamoto, T. Kamada, K. Onomitsu, I. Mahboob, H. Yamaguchi, Optical Tuning of Coupled Micromechanical Resonators, Appl. Phys. Express, 2 (2009) 062202.

[40] K. Ekinci, Y. Yang, M. Roukes, Ultimate limits to inertial mass sensing based upon nanoelectromechanical systems, J. Appl. Phys., 95 (2004) 2682-2689.

# Figure captions

**Fig. 1.** Proposed micromechanical resonator device: (a) Device overview of the doubly clamped beam. The gold nanorod absorber located at the center; (b) Top view of the gold nanorod array; (c) Absorber Cross-section.

**Fig. 2.** Schematic representation of detection experimental setup. The evaluation of the laser wavelength ranged from 1548 to 1562 nm.

**Fig. 3.** Temperature distributions of the resonator beam along the longitudinal direction depending on the beam length. A width of 20 μm, a thickness of 2 μm, and $\beta P$ of 0.4 mW were used in this calculation. The dotted line shows the theoretical results calculated by Eq. (1). The temperature of the fixed ends of the resonator beam was set to 300 K. The solid line shows the analytical results by FEM simulation.

**Fig. 4.** SEM images of: (a) overall micromechanical resonator with a beam length of 188 μm; (b) gold nanorod array from the top view; (c) magnified gold nanorods; (d) cross-sectional gold nanorod.

**Fig. 5.** Experimental optical absorption spectra. (a) Spectra of (i) the gold nanorod array (AuNR) on the gold thin film with the Si thin film (Si/AuNR/Au) (red line), (ii) Si thin film on the gold thin film (Si/Au) (blue line), and (iii) AuNR on the gold thin film without the Si thin film (AuNR/Au) (green line); (b) Enlarged view of the measured absorption spectrum of Si/AuNR/Au from 1530 to 1570 nm.

**Fig. 6.** Experimental results of the resonant frequency under no NIR laser irradiation depending on the beam length. The resonant frequencies were calculated using $f_0 = 1.03h/L^2\sqrt{E/\rho}$, as shown in Section 2.

**Fig. 7.** Frequency response of micromechanical resonator depending on the irradiated laser wavelength. The beam length and laser intensity were 188 μm and 1 mW, respectively.

**Fig. 8.** Resonant frequencies of two devices with and without a nanostructure as functions of the laser wavelength. The beam length and laser intensity were 188 μm and 1 mW, respectively.

**Fig. 9.** Relative resonant frequency shifts as a function of the laser wavelength. The beam length varied from 62 μm to 188 μm. The laser intensity was set to 1 mW.

**Fig. 10.** Relative resonant frequency shifts at a laser wavelength of 1558 nm depending on the beam length. The fitting results are shown as a dotted line.

**Fig. 11.** Resonant frequencies at a laser wavelength of 1558 nm depending on the evaluation laser intensity at a beam length of 188 μm.

# Figures

**Fig. 1**

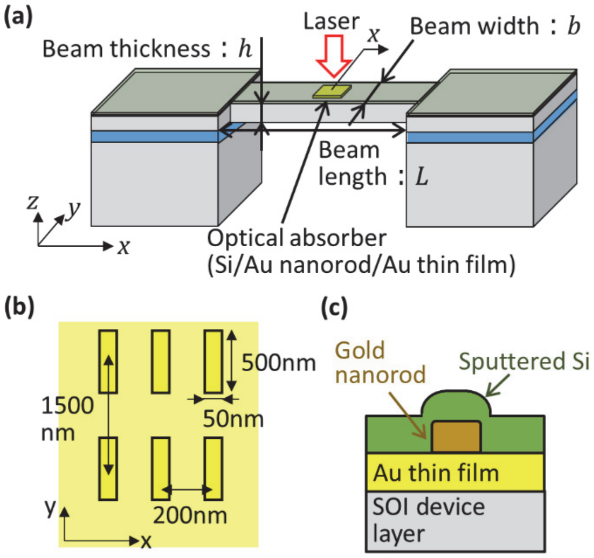

**Fig. 2**

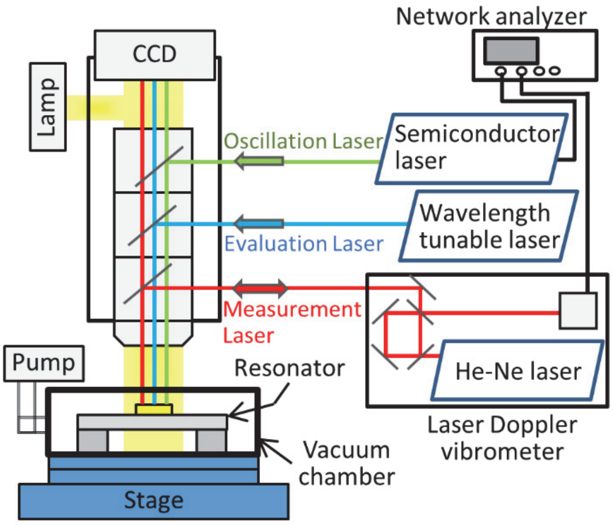

**Fig. 3**

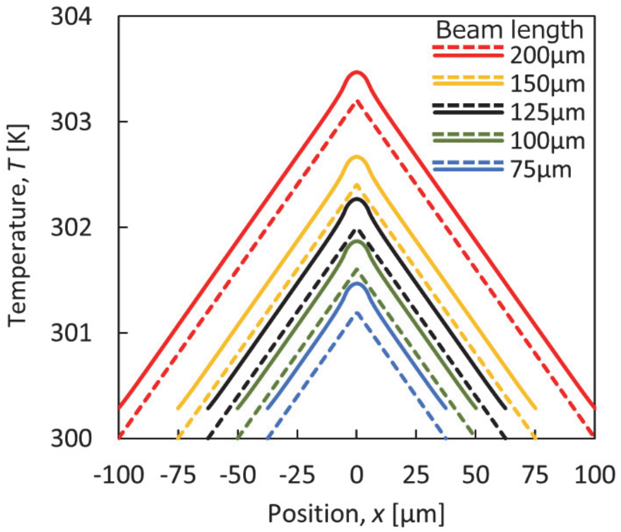
Beam length
200µm
150µm
125µm
100µm
75µm
Temperature, *T* [K]
304
303
302
301
300
-100
-75
-50
-25
0
25
50
75
100
Position, *x* [µm]

**Fig. 4**

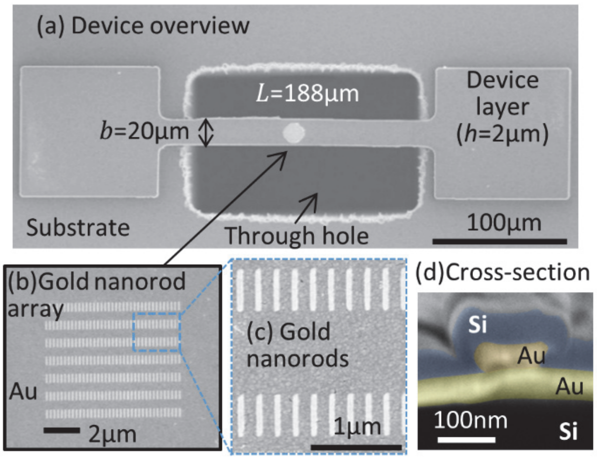
(a) Device overview
*L*=188µm
*b*=20µm
Device
layer
(*h*=2µm)
Substrate
Through hole
100µm
(b)Gold nanorod
array
Au
2µm
(c) Gold
nanorods
1µm
(d)Cross-section
Si
Au
Au
100nm
Si

**Fig. 5**

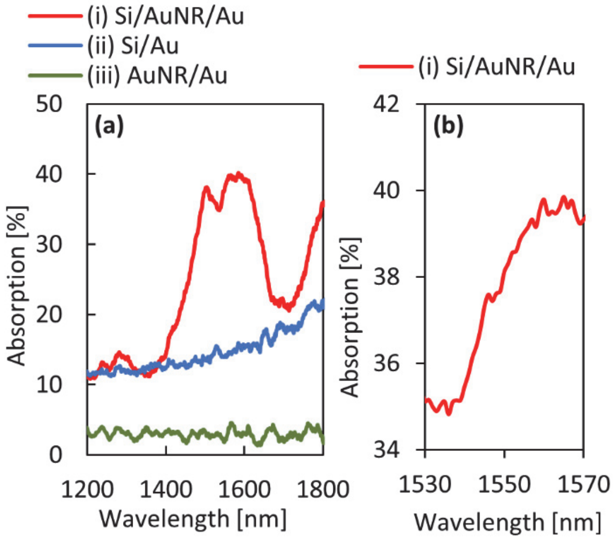
(i) Si/AuNR/Au
(ii) Si/Au
(iii) AuNR/Au
(a)
Absorption [%]
50
40
30
20
10
0
1200
1400
1600
1800
Wavelength [nm]
(i) Si/AuNR/Au
(b)
Absorption [%]
42
40
38
36
34
1530
1550
1570
Wavelength [nm]

**Fig. 6**

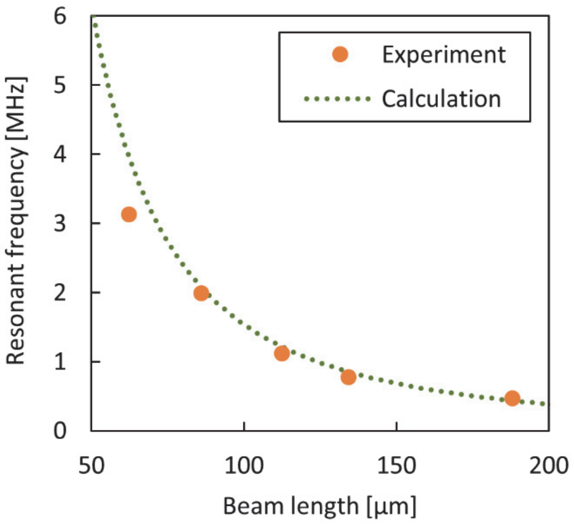
Experiment
Calculation
Resonant frequency [MHz]
6
5
4
3
2
1
0
50
100
150
200
Beam length [µm]

**Fig. 7**

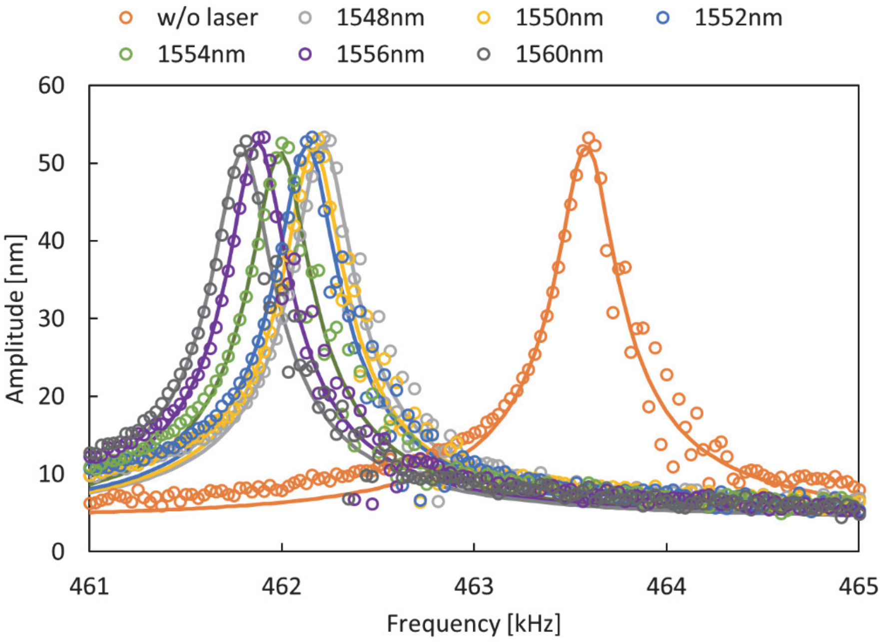
w/o laser
1548nm
1550nm
1552nm
1554nm
1556nm
1560nm
Amplitude [nm]
60
50
40
30
20
10
0
461
462
463
464
465
Frequency [kHz]

**Fig. 8**

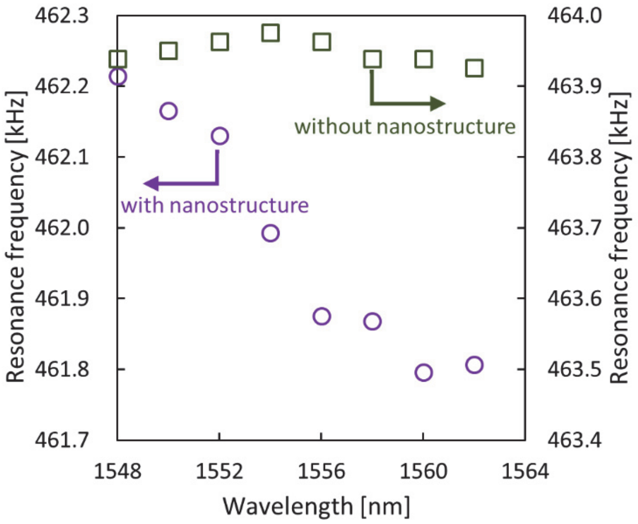
462.3
462.2
462.1
462.0
461.9
461.8
461.7
Resonance frequency [kHz]
464.0
463.9
463.8
463.7
463.6
463.5
463.4
Resonance frequency [kHz]
without nanostructure
with nanostructure
1548
1552
1556
1560
1564
Wavelength [nm]

**Fig. 9**

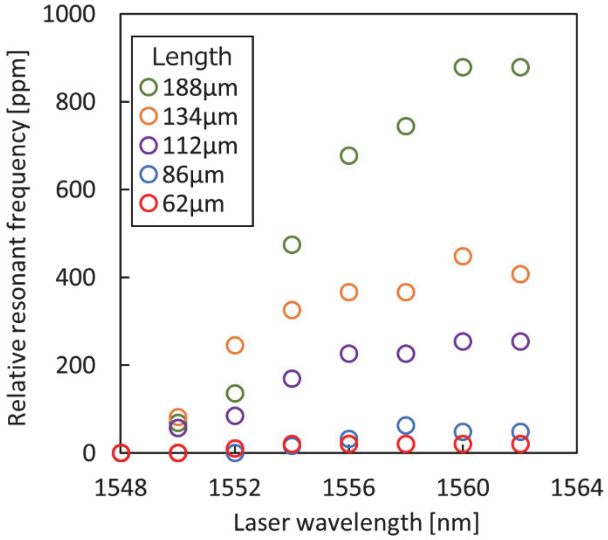
Length
188µm
134µm
112µm
86µm
62µm
Relative resonant frequency [ppm]
1000
800
600
400
200
0
1548
1552
1556
1560
1564
Laser wavelength [nm]

**Fig. 10**

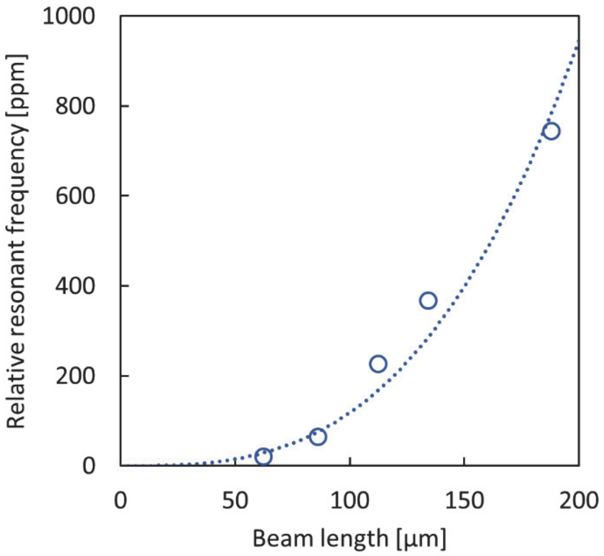
Relative resonant frequency [ppm]
1000
800
600
400
200
0
0
50
100
150
200
Beam length [µm]

**Fig. 11**

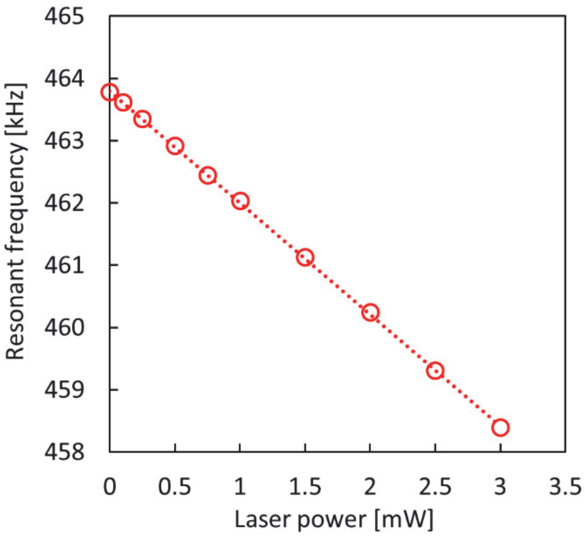
465
464
463
462
461
460
459
458
Resonant frequency [kHz]
0
0.5
1
1.5
2
2.5
3
3.5
Laser power [mW]